


# Tissue clearing techniques for three-dimensional optical imaging of intact human prostate and correlations with multi-parametric MRI

Stefano Cipollari MD<sup>1,2</sup> | Neema Jamshidi MD, PhD<sup>1,3</sup>  | Liutao Du MD, PhD<sup>3</sup> |  
Kyunghyun Sung PhD<sup>3</sup> | Danshan Huang MD<sup>3</sup> | Daniel J. Margolis MD<sup>4</sup> |  
Jiaoti Huang MD, PhD<sup>5</sup> | Robert E. Reiter MD<sup>6</sup> | Michael D. Kuo MD<sup>1</sup>

<sup>1</sup>Medical Artificial Intelligence Laboratory Program, The University of Hong Kong, Hong Kong, Hong Kong SAR

<sup>2</sup>Department of Radiology, La Sapienza, The University of Rome, Rome, Lazio, Italy

<sup>3</sup>Department of Radiological Sciences, David Geffen School of Medicine, University of California, Los Angeles, California, USA

<sup>4</sup>Department of Radiology, Cornell University, New York, New York, USA

<sup>5</sup>Department of Pathology, Duke University School of Medicine, Durham, North Carolina, USA

<sup>6</sup>Department of Urology, David Geffen School of Medicine, University of California, Los Angeles, California, USA

## Correspondence

Michael D. Kuo, MD, Medical Artificial Intelligence Laboratory Program, The University of Hong Kong, Hong Kong SAR.  
Email: [mikedkuo@gmail.com](mailto:mikedkuo@gmail.com)

## Funding information

National Cancer Institute, Grant/Award Number: 2P50CA092131; National Center for Advancing Translational Sciences, Grant/Award Number: KL2TR001882; Prostate Cancer Foundation, Grant/Award Number: Stewart Rahr-PCF Young Investigator Award

## Abstract

**Background:** Tissue clearing technologies have enabled remarkable advancements for in situ characterization of tissues and exploration of the three-dimensional (3D) relationships between cells, however, these studies have predominantly been performed in non-human tissues and correlative assessment with clinical imaging has yet to be explored. We sought to evaluate the feasibility of tissue clearing technologies for 3D imaging of intact human prostate and the mapping of structurally and molecularly preserved pathology data with multi-parametric volumetric MR imaging (mpMRI).

**Methods:** Whole-mount prostates were processed with either hydrogel-based CLARITY or solvent-based iDISCO. The samples were stained with a nuclear dye or fluorescently labeled with antibodies against androgen receptor, alpha-methylacyl coenzyme-A racemase, or p63, and then imaged with 3D confocal microscopy. The apparent diffusion coefficient and  $K^{trans}$  maps were computed from preoperative mpMRI.

**Results:** Quantitative analysis of cleared normal and tumor prostate tissue volumes displayed differences in 3D tissue architecture, marker-specific cell staining, and cell densities that were significantly correlated with mpMRI measurements in this initial, pilot cohort.

**Conclusions:** 3D imaging of human prostate volumes following tissue clearing is a feasible technique for quantitative radiology-pathology correlation analysis with mpMRI and provides an opportunity to explore functional relationships between cellular structures and cross-sectional clinical imaging.

## KEYWORDS

CLARITY, iDISCO, prostate, prostate cancer, radiogenomics, tissue clearing

Cipollari and Jamshidi are co-first authors.

**Abbreviations:** ADC, apparent diffusion coefficient; AR, androgen receptor; FFPE, formalin-fixed paraffin embedded; H/E, hematoxylin and eosin; mpMRI, multi-parametric magnetic resonance imaging; PBS, phosphate-buffered saline; PI, propidium iodide; SDS, sodium dodecyl sulfate.

## 1 | BACKGROUND

The noninvasive extraction of detailed structural and molecular information from intact biological systems remains a fundamental goal of medical imaging. Current methods of medical image interpretation rely on the correlation between large imaging datasets encoding for both macroscopic structural, functional, and dynamic information relative to large tissue volumes, and thin-section histopathology slides. Histology sections, however, at an average thickness of 5  $\mu\text{m}$ , are insufficient for any assessment of volumetric cell–cell interactions. Furthermore, extensive molecular phenotyping is challenging to achieve within tissue sections due to a limited ability to evaluate more than a handful of molecular markers on the same slide and due to difficulty to spatially distinguish signals in cases of overlapping cells.<sup>1,2</sup> Thus, new methods enabling more extensive spatial mapping of medical image datasets against larger and intact tissue specimens at a structural as well as molecular level are needed and represent a critical next step in the advancement of medical imaging.

As an attempt to reduce refractive index interfaces within tissues, the main barrier to the achievement of detailed microscopic imaging of intact volumes,<sup>3–5</sup> pioneering techniques have been developed starting in the early 1900s.<sup>6</sup> Recently, thanks to the development of technologies such as CLARITY<sup>7</sup> and iDISCO,<sup>8</sup> researchers are able to extract high-resolution structural and molecular data from intact tissue volumes.<sup>7,9–15</sup> CLARITY combines hydrogel-based tissue embedding and lipid extraction via electrophoresis or incubation in detergent to homogenize the refractive index of the tissues, while iDISCO uses dehydration and organic solvents to remove lipids. Precise visual mapping and quantification of potentially any molecular structure across the entirety of the specimen with the sub-micron resolution are also possible via the use of endogenous fluorescence or immunolabeling.<sup>7,8</sup>

A cornerstone of modern diagnostic medicine involves the radiology–pathology (Rad–Path) correlation;<sup>16</sup> in the 21st century, bringing this to bear in the context of advanced measurement capabilities in noninvasive and tissue-based measurements, will be critical. Concurrently developments in clinical tomographic imaging have improved spatial resolution and improved capabilities to measure tissue and organ functional information, beyond just anatomical structures. Radiogenomics was developed to help bridge the divide between molecular phenotypes and clinical imaging phenotypes, through concordant use of omic data, histological data, clinical imaging, and clinical diagnoses/outcomes.<sup>17–25</sup> Now, the availability of clearing techniques can potentially allow one to establish new quantitative three-dimensional (3D) radiogenomic correlations of intact tissue volumes, preserving spatial relationships across multiple orders of magnitude, from a systems-level of tissue organization down to subcellular resolution.

Herein, we present a preliminary study aimed at demonstrating the feasibility of a novel radiogenomic approach capable of extending Rad–Path correlations to intact tissue volumes. In this study, we link 3D volumetric tissue data with structural and molecular information

from human prostate samples cleared using CLARITY<sup>7</sup> or iDISCO<sup>8</sup> and multi-parametric magnetic resonance imaging (mpMRI<sup>26</sup>).

## 2 | METHODS

### 2.1 | Patients and samples

Whole-mount formalin-fixed paraffin-embedded (FFPE) prostate samples from patients with prostate cancer who underwent radical prostatectomy at UCLA between May 2014 and July 2014 were obtained. Patients who had available high quality (i.e., free from artifacts and adequate for further imaging postprocessing) matching preoperative mpMRI were included for radiogenomic analysis. Thick sections of approximately 100  $\mu\text{m}$  (20 times thicker than conventional histology) were cut from each sample and then cleared as described below. Adjacent thin-section (5  $\mu\text{m}$  thick) hematoxylin and eosin slides (H/E) were obtained; specific regions of interest within a whole-mount were first manually delineated by the genitourinary pathologist (20 years genitourinary pathology experience) and then verified on both slides for histologic similarity.

### 2.2 | Tissue clearing, staining, and imaging

One sample was processed using the CLARITY procedure as previously described.<sup>7,11</sup> Briefly, the paraffin-embedded slide was deparaffinized, rehydrated, and then incubated with hydrogel monomer solution. The tissue–hydrogel matrices were washed with phosphate-buffered saline (PBS) and then incubated with sodium dodecyl phosphate (SDS) and SDS buffer. The sample was washed with PBS and incubated with primary antibodies (rabbit anti-human androgen receptor [AR]; Cell Signaling), then washed with PBS and incubated with secondary antibodies (Fab fragment secondary anti-rabbit-Alexa593 antibodies; Cell Signaling). Nuclei were labeled with propidium iodide (PI; Invitrogen). The samples were incubated with in refractive index matching solution and then mounted onto slides.

Two samples were processed with the iDISCO procedure published by Renier et al.<sup>8</sup> Briefly, the fixed samples were first incubated with a series of methanol, bleached with 5%  $\text{H}_2\text{O}_2$ , and then sequentially washed in methanol, dimethyl sulfoxide, PBS, and PBS/0.2% Triton X-100. The samples were incubated with primary antibodies (mouse anti-human alpha-methylacyl coenzyme-A racemase [AMACR]; Thermo Fisher Scientific, and rabbit anti-human p63- $\alpha$  [p63]; Cell Signaling) and with secondary antibody incubation (Cell Signaling). The samples were then washed in PTwH buffer (0.2% Tween in PBS with 10  $\mu\text{g}/\text{ml}$  heparin), stained with PI (Invitrogen), and finally cleared with a simplified version of 3DISCO<sup>10</sup> and mounted on a chamber filled with dibenzyl ether (Sigma-Aldrich). Further details on the sample processing are available in the Supporting Information Materials.

Images were acquired using a Leica SP5 confocal microscope equipped with dry 10X and water-immersion 20X objectives. Imaris

software (Bitplane) was used for visualization. Given the clarity and relatively uniform density of nuclear staining, cell density estimates were performed via nuclear segmentation with marker-controlled watershed<sup>27</sup> spot segmentation of nuclei as implemented in Imaris (Bitplane). Seed point diameter estimates were specified at different ranges (to avoid issues related to over or under segmentation as a result of variation of different size nuclei due to asynchrony of the cell cycle for the different cells) for nuclear cellular sizes from 4.5 to 6  $\mu\text{m}$  in 0.2  $\mu\text{m}$  increments for the nuclear-stained-filtered images.

## 2.3 | MRI protocol and postprocessing

All cases underwent preoperative mpMRI on 3T systems (MAGNETOM Skyra and MAGNETOM Trio; Siemens Medical Systems) using a body array matrix and spine array coil. The standard clinical mpMRI protocol was used, including axial and coronal turbo spin-echo T2-weighted (T2w), axial echo-planar diffusion-weighted imaging (DWI), and axial dynamic contrast-enhanced MRI (DCE-MRI). Apparent diffusion coefficient (ADC;  $\mu\text{m}^2/\text{s}$ ),  $K^{\text{trans}}$  (influx volume transfer coefficient;  $\text{min}^{-1}$ ), and  $k^{\text{ep}}$  (outflux volume transfer coefficient;  $\text{min}^{-1}$ ) were obtained from DWI and DCE-MRI data.

ADC maps were created by using the in-line postprocessing software (Siemens Medical Systems) by using linear least squares curve fitting of pixels (log scale) in the four DWI images against their corresponding  $b$ -values (0/100/400/800). The following mono-exponential decay model was used:  $S = S_0 \times \exp(-b \times \text{ADC})$ , where  $S$  and  $S_0$  are the pixel values with and without applying a  $b$ -value of diffusion sensitive gradients.

DCE-MRI images were acquired before, during, and after a single-dose injection of gadopentetate dimeglumine (Magnevist) at a dose of 0.1 mmol/kg through a peripheral vein at a rate of 2 ml/s via a mechanical injector. The DCE-MRI acquisition consisted of a fast 3D RF-spoiled gradient-echo sequence, with a phase direction from left to right without fat saturation. About 9–10 unenhanced sets (total acquisition time, around 40 s) and approximately 65 contrast-enhanced sets of images were acquired sequentially without a delay between acquisitions. A total of 1500 images were obtained during DCE-MRI. DCE-MRI images were evaluated by using parametric maps, processed by a separate workstation (OmniLook iCAD Inc). The color-coded parametric maps,  $K^{\text{trans}}$  (wash-in) and  $k^{\text{ep}}$  (wash-out) were obtained by a two-compartment pharmacokinetic (standard Tofts) model.<sup>28</sup> For 3D imaging, the maximum intensity projection was applied to the manually segmented prostate.

## 2.4 | Rad-Path correlations of intact prostate tissue and mpMRI

Cognitive registration was jointly performed by the pathologist and radiologist to map matched normal and tumor samples between H/E slides, cleared tissue volume samples and MRI images on the basis of zonal anatomy and identifiable imaging landmarks. AMACR staining

of the 3D tissue images was assessed with binary presence/absence determinations by the pathologist (J. H). Segmented cell counts were performed on the cleared tissue images throughout the sampled regions on a voxel-wise basis using the Imaris software (Bitplane).  $t$ -test calculations were performed for cellular density, ADC, and  $K^{\text{trans}}$  comparisons between tumor and normal tissue areas with significance criteria  $p < .05$ . If the  $F$ -test for variance equality was significantly different between the measurements then Welch's  $t$ -test was used, otherwise, Student's  $t$ -test was used. The measured quantities were plotted as box plots with the interquartile (IQR) percentage and whiskers at  $\pm 1.5 \times \text{IQR}$ .

## 3 | RESULTS

### 3.1 | Patients and samples

This study involved retrospective analysis according to an institutional review board-approved, Health Insurance Portability and Accountability Act protocol permitting evaluation of resected tissue specimens and diagnostic imaging studies. Five patients with prostate cancer and available whole-mount prostate samples suitable for tissue clearing with matching preoperative multi-parametric MR images were identified. Two patients were excluded due to the inadequate quality of the preoperative MR studies. The mean age of the remaining patients was  $59 \pm 9$  years. Patients 1 and 2 had unifocal Gleason 4 + 3 prostate cancer and Patient 3 had multifocal prostate cancer (Gleason 4 + 3, 3 + 3, and 3 + 3).

### 3.2 | Tissue clearing, staining, and imaging

All three samples were successfully cleared, stained, and visualized using either CLARITY or iDISCO. Our first goal was to establish the feasibility of implementing CLARITY with FFPE whole-mount prostate glands. We selected a thick-section (100  $\mu\text{m}$ ) of nontumor, normal glandular tissue from the whole-mount gland in the first patient (Patient 1), a 55-year-old male with a unifocal Gleason 4 + 3 prostate cancer. Applying CLARITY, we were able to clear the tissue and make it optically transparent with minimal tissue distortion ( $<10\%$ /unit area) with no significant tissue loss (Figure 1A). The sample was subsequently double-stained with anti-AR antibodies and the nuclear dye and then imaged at 10X, revealing good fluorescent signal uniformly present throughout the thickness of the sample from both AR-stained cells and stained nuclei as well as good preservation and visualization of prostate glandular structures (Figures 1B and S1). The same matched areas of the whole mount imaged with CLARITY and with conventional microscopy (on the adjacent H/E slide) revealed comparable glandular appearance, typical of normal prostate (Figure 1B).

Next, we applied the alternative solvent-based iDISCO method on the second sample (Patient 2), a 53-year-old male with unifocal Gleason 4 + 3 prostate cancer. We similarly selected a thick-section

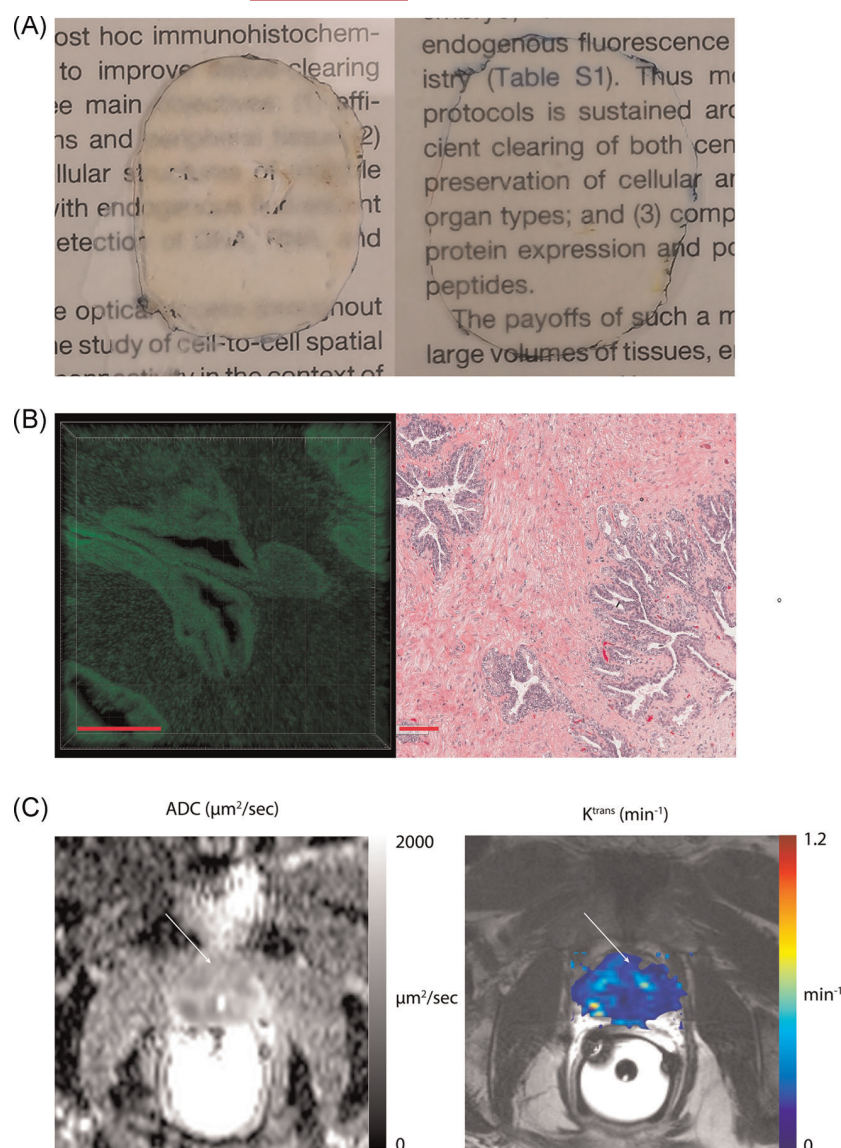


**FIGURE 1** CLARITY sample processing and normal tissue imaging. Patient 1 is a 55-year-old male with Gleason 4 + 3 prostate cancer. (A) Whole-mount 100µm thick section before (left) and after (right) clearing with CLARITY. (B) Normal glandular structures from the same area are shown in the volumetric confocal images (left) and on the adjacent thin section H/E slide (right), revealing similar architectural features. The green signal in the CLARITY image is the fluorescently labeled antibody anti-AR. (C) Multiparametric-MRI with ADC (left) and  $K^{trans}$  (right) maps. The white arrows point at the areas shown in (B) ADC, and  $K^{trans}$  values in these areas are suggestive of normal prostate tissue. In contrast, the red arrows indicate regions of low ADC and high  $K^{trans}$  in the right posterior aspect of the gland, corresponding to Gleason 4 + 3 prostate cancer nodules. The ADC and  $K^{trans}$  color codes appear along the right-most column, corresponding to black and white  $0.2000 \mu^2/s$  and rainbow  $0.12 \text{ min}^{-1}$ , respectively. Scale bars = 100 µm. ADC, apparent diffusion coefficient; AR, androgen receptor; H/E, hematoxylin and eosin; MRI, magnetic resonance imaging [Color figure can be viewed at [wileyonlinelibrary.com](http://wileyonlinelibrary.com)]

(100 µm) whole-mount sample of nontumor, normal glandular tissue from the whole-mount gland. iDISCO was also able to clear the thick section of normal prostate glandular tissue without apparent tissue loss or distortion (Figure 2). The sample was then double-stained with the basal cell-specific anti-p63 antibody<sup>29,30</sup> and the nuclear dye. The homogenous signal was detected from both the anti-p63 antibody and the nuclear dye throughout the entire thickness of the specimen. Again, normal glandular structures were clearly identifiable and similar in appearance compared to the adjacent H/E thin slide, without architectural distortion (Figure 2). Compared to CLARITY, iDISCO provided a higher signal-to-noise ratio, while total sample processing was twice as fast (2 vs. 5.5 weeks).

Based on these initial results we used iDISCO for processing the tissue from the third sample (Patient 3), a 69-year-old patient with multifocal prostate cancer (Gleason 4 + 3, 3 + 3, 3 + 3 for the three foci, respectively). This time our goal was to evaluate tumor regions in the whole-mount gland, we, therefore, selected a tissue volume

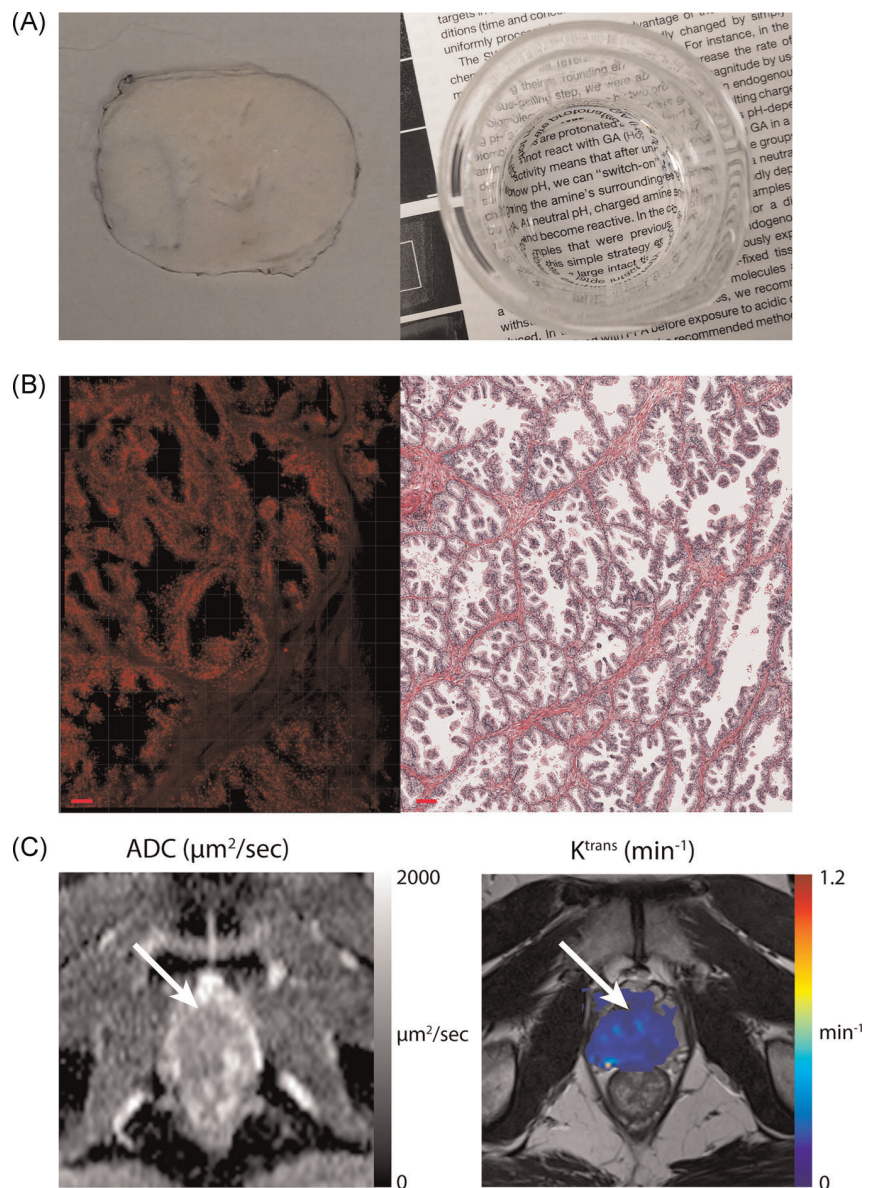
(100 µm) containing both cancer and noncancer areas in the same sample. After applying the immunofluorescent antibody against AMACR, a known tissue marker of prostate cancer,<sup>31–33</sup> and the nuclear staining, the processed sample was imaged using 10X (Figure 3B) and 20X (Figures 3C and S2) lenses. The image quality and the fluorescent signal were overall comparable to the previous iDISCO sample (Figures 3 and S2). Differences in tissue architecture were evident in both low- and high-power images between normal and tumor areas (Figure 3B,C), with similar tissue characteristics to the matched regions on the adjacent H/E slide.

### 3.3 | Rad-Path correlations of intact prostate tissue and mpMRI

Having established our ability to clear thick section prostate samples, and to apply both intrinsic and immune-labeled stains, we next



**FIGURE 2** iDISCO sample processing and normal tissue imaging. Patient 2 is a 53-year-old male with Gleason 4 + 3 prostate cancer. (A) Whole-mount 100- $\mu\text{m}$  thick section before (left) and after (right) clearing using iDISCO. (B) Normal prostate glands from the same prostate area are shown on the thick iDISCO-processed section (left) and on the adjacent H/E slide (right). Similarities in tissue architecture are evident between the two techniques. The red signal from the volume images is the antibody anti-p63. (C) mpMRI images showing ADC (left) and  $K^{\text{trans}}$  (right) maps. The white arrows point in the ADC and  $K^{\text{trans}}$  correspond to the histological regions in (B), reflecting concordance between histology and mpMR for normal prostate. Scale bars = 100  $\mu\text{m}$ . ADC, apparent diffusion coefficient; H/E, hematoxylin and eosin; mpMRI, multi-parametric magnetic resonance imaging [Color figure can be viewed at [wileyonlinelibrary.com](http://wileyonlinelibrary.com)]



performed a two-step analysis first descriptively comparing quantitative mpMRI parameters, including ADC and  $K^{\text{trans}}$ , to the qualitative intact tissue characteristics of the matched prostate samples after clearing in all three patients, and then quantitatively correlating mpMRI parameters with automatically extracted cell count data from normal and tumor areas for Patient 3. For Patients 1 and 2, high ADC and low  $K^{\text{trans}}$  values and T2w signal iso-intensity were registered in the normal gland areas imaged on the cleared thick sections (Figures 1C and 2C), which were consistent with mpMRI features of normal prostate.<sup>34–39</sup> The microscopic appearance and architecture of the gland and presence, distribution and gross quantity of nuclear, p63 and AR staining in the matching regions on the cleared volume samples (confirmed by pathological analysis) were consistent with normal prostate glandular tissue and consistent with expected findings from the H/E slides of normal prostate glands for Patients 1 and 2.

We next performed a quantitative analysis comparing normal and tumor tissue regions in Patient 3. mpMRI maps relative to a portion of the main tumor focus (Gleason 4 + 3; Figure 3D) showed statistically significant differences between prostate cancer and normal tissue ( $\text{ADC} = 826.8 \pm 89.9$  vs.  $1839.2 \pm 67.0 \mu\text{m}^2/\text{s}$ ;  $p = 8.57 \times 10^{-15}$  by Student's *t*-test and  $K^{\text{trans}} = 0.358 \pm 0.083$  vs.  $0.138 \pm 0.011 \text{ min}^{-1}$ ;  $p = 3.81 \times 10^{-5}$  by Welch's *t*-test; Figure 4C), indicative of differences in higher cell density and tissue perfusion consistent with typical features of prostate cancer.<sup>34–39</sup> 3D volume images of the cleared tissue reflected the regional differences observed by mpMRI with significantly increased cellular density ( $6353 \pm 923$  cells/ $\mu\text{m}^3$  vs.  $4401 \pm 924$  cells/ $\mu\text{m}^3$ ;  $p = .0019$  by Student's *t*-test) as well as positive AMACR staining in the tumor region relative to the adjacent normal region (Figures 3 and 4). Quantitative analysis revealed a statistically significant difference in cell density between normal and tumor areas on the cleared sample

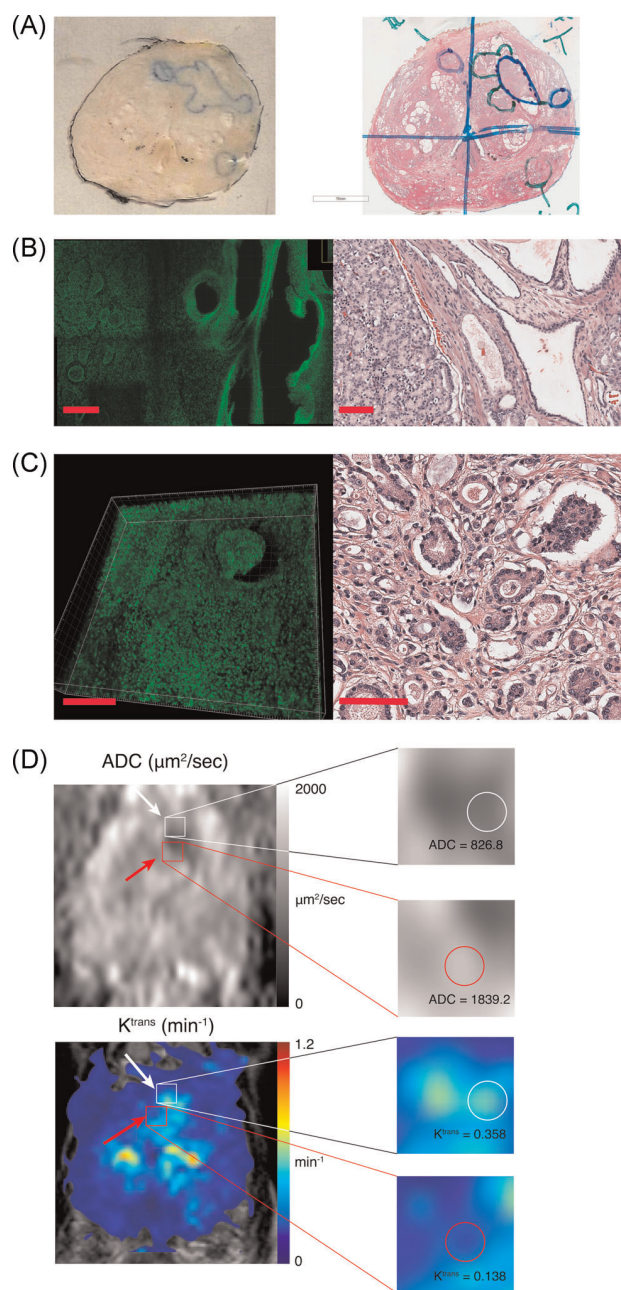


**FIGURE 3** (See caption on next column)

( $p = .0019$ ; Figure 4C), consistent with the differences in ADC and  $K^{\text{trans}}$  between the same matched normal and tumor areas (3D MIP imaging of T2-weighted MRI, ADC maps, and  $K^{\text{trans}}$  maps for Patient 3 are available in the Supporting Information Materials).

## 4 | DISCUSSION

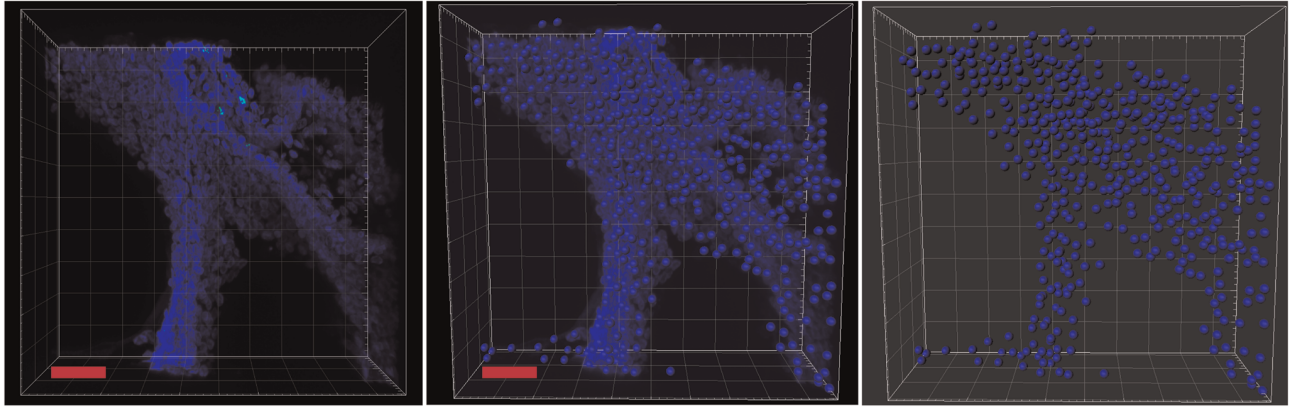
In this study, we demonstrate the feasibility of complete tissue clearing and subsequent cellular and molecular phenotyping of whole-mount prostate samples twenty times thicker than traditional histology using CLARITY<sup>7</sup> and iDISCO<sup>8</sup> in normal and cancer specimens. We then show that quantitative and qualitative mpMRI features are concordant with the features seen on the cleared intact prostate volumes as well as traditional H/E thin sections. Finally, quantitative analysis of cellular count data from the cleared tissue volumes revealed significant differences between normal and tumor areas, which were mirrored by differences in  $K^{\text{trans}}$  and ADC.

These initial results show the validity and usefulness of tissue clearing for the 3D microscopic imaging of the human prostate and the potential impact of applying them as a tool for the advancement of the Rad-Path correlation assessment. In this setting, the recent developments in tissue clearing technologies present the opportunity to obtain a radiogenomic map of spatially preserved structural, molecular, and functional information from intact tissue specimens. Compared to the traditional 2D-based approach, a volume-based analysis allows for an improved genotypic-phenotypic understanding of spatial relationships spanning multiple orders of magnitude and can potentially be applied to almost any clinical imaging setting in

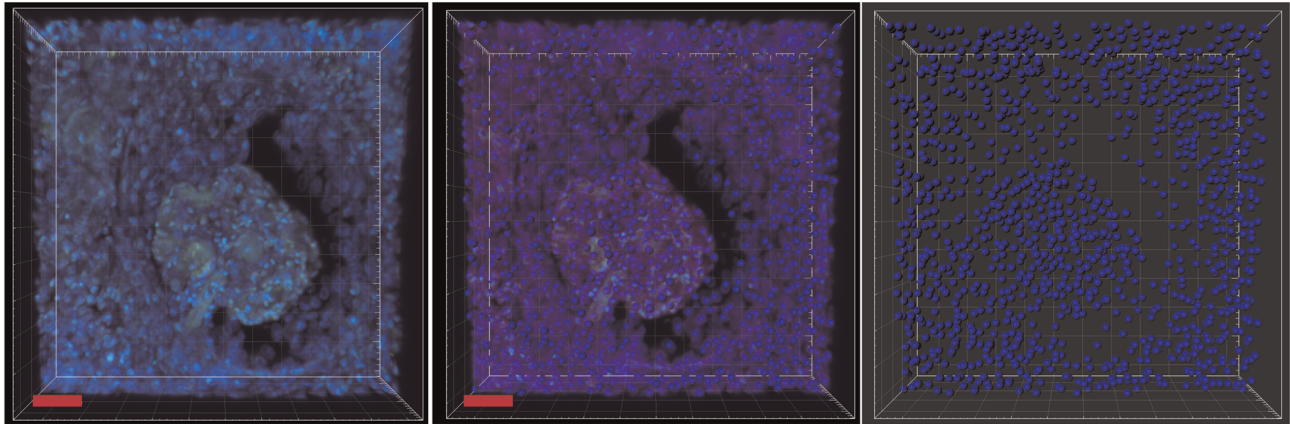
**FIGURE 3** iDISCO sample showing regional architectural differences in normal versus tumor areas and correlations with mpMRI. Patient 3 is a 69-year-old male with multifocal prostate cancer. (A) Whole-mount 100  $\mu\text{m}$  thick prostate sample before iDISCO processing (left) and corresponding adjacent H/E thin section (right). (B) Low power (10X) images of both the iDISCO volume sample (left) and the thin H/E slide (right) showing a transition area between normal tissue (on the right of the field of view) and tumor (on the left of the field of view). (C) High power (20X) images of a tumor area on the iDISCO (left) and H/E (right) samples. The green signal on the iDISCO image is the antibody anti-AMACR. Both the H/E and the cleared tissue volume images show similar tissue organization and cellular density. (D) mpMR images with ADC (top) and  $K^{\text{trans}}$  (bottom) maps. The white and red arrows indicate prostate cancer and normal tissue, respectively. The zoomed-in multi-parametric maps show clear differences between prostate cancer and normal tissue (ADC = 826.8 vs. 1839.2 and  $K^{\text{trans}} = 0.358$  vs. 0.138), indicative of differences in higher cell density and tissue perfusion, consistent with typical imaging features of prostate cancer. The ADC and  $K^{\text{trans}}$  color codes appear along the rightmost column, corresponding to black and white 0–2000  $\mu^2/\text{s}$  and rainbow 0–1.2  $\text{min}^{-1}$ , respectively. Scale bars = 100  $\mu\text{m}$ . ADC, apparent diffusion coefficient; H/E, hematoxylin and eosin; mpMRI, multi-parametric magnetic resonance imaging [Color figure can be viewed at [wileyonlinelibrary.com](http://wileyonlinelibrary.com)]



(A)



(B)



(C)

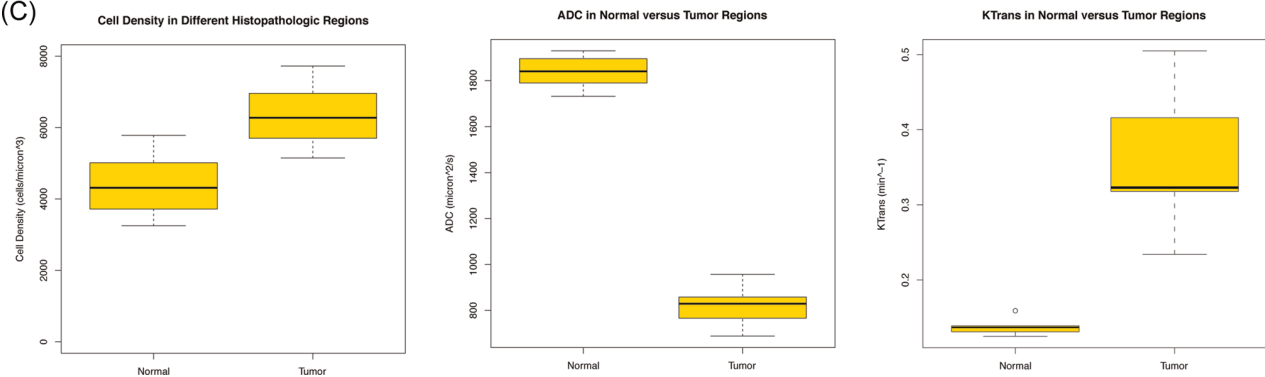


**FIGURE 4** Quantitative analysis of normal versus tumor areas in Patient 3. Normal prostate glands (A) and a tumor area (B) with a mass infiltrating a glandular duct from Patient 3 are shown. The left panels in (A) and (B) reveal differences in AMACR (green) signal. The central panels in (A) and (B) show both the fluorescent signal and the segmented nuclei, while the right panels only show the segmented nuclei. (C) Boxplot showing significantly different cellular densities in the normal versus tumor areas (left,  $p = .0019$ , Student's  $t$ -test,  $F = 1$ ). The central and right panels in (C) show differences in terms of ADC ( $p = 8.57 \times 10^{-15}$ , Student's  $t$ -test,  $F = 0.6$ ) and  $K^{\text{trans}}$  ( $p = 3.81 \times 10^{-5}$ , Welch's  $t$ -test,  $F = 0.02$ ) in the corresponding matched normal and tumor areas. Scale bars =  $30 \mu\text{m}$ . ADC, apparent diffusion coefficient; AMACR, alpha-methylacyl coenzyme-A racemase [Color figure can be viewed at [wileyonlinelibrary.com](http://wileyonlinelibrary.com)]

which imaging-tissue correlation is possible. The advantages of this new radiogenomic approach, however, extend beyond the simple possibility to more precisely analyze and correlate 3D structures seen by imaging. The compatibility of next-generation clearing techniques with immunofluorescent labeling also allows one to generate detailed in situ 3D molecular portrayals of cells, organelles, peptides, and even nucleic acids on the same samples while preserving their spatial arrangements.<sup>40,41</sup> Multiple rounds of molecular labeling are also possible on the same tissue volume increases the number of structures that can be targeted, which is not possible with standard immunohistochemical techniques.<sup>7,40</sup> Volume-based radiogenomic analysis thus potentially provides a crucial missing link between 3D structural and functional observations captured with noninvasive imaging, and the actual topography of constituent tissue structures, cancer cells, and their local microenvironment, allowing direct visualization of intratumoral heterogeneity across the intact tumor volume.<sup>42–44</sup> As new methods and variations of existing protocols are developed, we expect further improvements in technical and efficiency of tissue clearing.<sup>4</sup> For example, iDISCO provides a significant processing time advantage over CLARITY. Additionally, the transient tissue expansion that may occur with CLARITY is not seen in iDISCO, to the contrary, there is a small amount of shrinkage.<sup>5</sup>

The small sample size (three patients and a single cancer sample) is clearly a limitation that necessitates future studies involving larger cohorts, ideally prospectively, in a manner that allows more comprehensive evaluation of specificity and sensitivity, before being applied in a clinical context. Thus, these results are presented as an initial study demonstrating the feasibility and potential utility of the approach and measurements. Additionally, there are limitations inherent to the currently available tissue clearing technologies, complicating the achievement of complete 3D imaging of very large-volume tissues, including long sample processing and imaging times, relatively limited depth of antibody penetration through the sample, and the nontrivial cost. Further limitations of this study lie in the small thickness of the samples relative to the larger thickness of the MRI slices, as well as the small number of specimens and antigens evaluated. However there continues to be technical advancements enabling shorter tissue processing times as well as deeper penetration of tissues allowing for larger specimens, thus in the foreseeable future, this approach can be applied to larger volumes, different tissue types, molecular stains, and different computational approaches for mapping and registration, with a potential to significantly impact the diagnostic characterization of tissue specimens.

## 5 | CONCLUSION

In summary, we demonstrate the feasibility of a novel integrative imaging approach that enables 3D spatially preserved correlations across multiple spatial scales. This could have an enormous impact upon multiple dimensions of investigation including but not limited to improving understanding of histopathology and radiology correlates

of normal and diseased tissues, as well as providing a powerful means to better understand cellular and genomic spatial heterogeneity.

## ACKNOWLEDGMENTS

Neema Jamshidi was supported by the Prostate Cancer Foundation (the Stewart Rahr-PCF Young Investigator Award) and a NIH NCATS and NIBIB UCLA CTSI Grant Number KL2TR001882 (PD: Wong). Michael D. Kuo and Neema Jamshidi were supported by UCLA Prostate Cancer Spore Career Development Award (NCI SPORE 2P50CA092131).

## CONFLICT OF INTERESTS

The authors declare that there are no conflict of interests.

## AUTHOR CONTRIBUTIONS

Stefano Cipollari drafted the manuscript. Neema Jamshidi analyzed the results. Liutao Du and Danshan Huang performed tissue experiments. Kyunghyun Sung performed MR measurements. Jiaoti Huang performed histological measurements. Michael D. Kuo conceived of the study and its design. All authors edited the manuscript and agreed upon the final content.

## DATA AVAILABILITY STATEMENT

All data generated or analyzed during this study are included in this published article and its Supporting Information Files.

## ETHICS STATEMENT

This study involved retrospective analysis according to an institutional review board-approved, Health Insurance Portability and Accountability Act protocol permitting evaluation of resected tissue specimens and diagnostic imaging studies.

## ORCID

Neema Jamshidi  <https://orcid.org/0000-0003-3857-9735>

## REFERENCES

1. Insel TR, Young LJ. The neurobiology of attachment. *Nat Rev Neurosci*. 2001;2(2):129-136.
2. Mombaerts P, Wang F, Dulac C, Chao SK, Nemes A, Mendelsohn M. Visualizing an olfactory sensory map. *Cell*. 1996; 87(4):675-686.
3. Richardson DS, Lichtman JW. Clarifying tissue clearing. *Cell*. 2015; 162(2):246-257.
4. Azaripour A, Lagerweij T, Scharfbillig C, Jadczyk AE, Willershausen B, Van Noorden CJ. A survey of clearing techniques for 3D imaging of tissues with special reference to connective tissue. *Prog Histochem Cytochem*. 2016;51(2):9-23.
5. Yu T, Qi Y, Gong H, Luo Q, Zhu D. Optical clearing for multiscale biological tissues. *J Biophotonics*. 2018;11:2.
6. Spalteholz W. *Über das Durchsichtigmachen von menschlichen und tierischen Präparaten und seine theoretischen Bedingungen, nebst Anhang: Über Knochenfärbung*. Leipzig: S. Hirzel; 1914.
7. Chung K, Wallace J, Kim SY, Kalyanasundaram S, Andalman AS, Davidson TJ. Structural and molecular interrogation of intact biological systems. *Nature*. 2013;497(7449):332-337.
8. Renier N, Wu Z, Simon DJ, Yang J, Ariel P, Tessier-Lavigne M. iDISCO: a simple, rapid method to immunolabel large tissue samples for volume imaging. *Cell*. 2014;159(4):896-910.



9. Dodt H-U, Leischner U, Schierloh A, Jahrling N, Mauch CP, Deininger K. Ultramicroscopy: three-dimensional visualization of neuronal networks in the whole mouse brain. *Nat Meth.* 2007;4(4):331-336.
10. Erturk A, Lafkas D, Chalouni C. Imaging cleared intact biological systems at a cellular level by 3DISCO. *J Vis Exp.* 2014;(89):51382. <https://doi.org/10.3791/51382>
11. Tomer R, Ye L, Hsueh B, Deisseroth K. Advanced CLARITY for rapid and high-resolution imaging of intact tissues. *Nat Protoc.* 2014;9(7):1682-1697.
12. Yang B, Treweek JB, Kulkarni RP, et al. Single-cell phenotyping within transparent intact tissue through whole-body clearing. *Cell.* 2014;158(4):945-958.
13. Kuwajima T, Sitko AA, Bhansali P, Jurgens C, Guido W, Mason C. ClearT: a detergent- and solvent-free clearing method for neuronal and non-neuronal tissue. *Development.* 2013;140(6):1364-1368.
14. Hua L, Zhou R, Thirumalai D, Berne BJ. Urea denaturation by stronger dispersion interactions with proteins than water implies a 2-stage unfolding. *Proc Natl Acad Sci U S A.* 2008;105(44):16928-16933.
15. Susaki EA, Tainaka K, Perrin D, et al. Whole-brain imaging with single-cell resolution using chemical cocktails and computational analysis. *Cell.* 2014;157(3):726-739.
16. Murphey MD, Madewell JE, Olmsted WW, Ros PR, Neiman HL. A history of radiologic pathology correlation at the Armed Forces Institute of Pathology and its evolution into the American Institute for Radiologic Pathology. *Radiology.* 2012;262(2):623-634.
17. Diehn M, Nardini C, Wang DS, et al. Identification of noninvasive imaging surrogates for brain tumor gene-expression modules. *Proc Natl Acad Sci U S A.* 2008;105(13):5213-5218.
18. Segal E, Sirlin CB, Ooi C, et al. Decoding global gene expression programs in liver cancer by noninvasive imaging. *Nature Biotechnol.* 2007;25(6):675-680.
19. Yamamoto S, Huang D, Du L, et al. Radiogenomic analysis demonstrates associations between (18)F-fluoro-2-deoxyglucose PET, prognosis, and epithelial-mesenchymal transition in non-small cell lung cancer. *Radiology.* 2016;280(1):261-270.
20. Jamshidi N, Jonasch E, Zapala M, et al. The radiogenomic risk score stratifies outcomes in a renal cell cancer phase 2 clinical trial. *Eur Radiol.* 2016;26(8):2798-2807.
21. Yamamoto S, Han W, Kim Y, et al. Breast cancer: radiogenomic biomarker reveals associations among dynamic contrast-enhanced MR imaging, long noncoding RNA, and metastasis. *Radiology.* 2015;275(2):384-392.
22. Jamshidi N, Jonasch E, Zapala M, et al. The radiogenomic risk score: construction of a prognostic quantitative, noninvasive image-based molecular assay for renal cell carcinoma. *Radiology.* 2015;277(1):114-123.
23. Yamamoto S, Korn RL, Oklu R, et al. ALK molecular phenotype in non-small cell lung cancer: CT radiogenomic characterization. *Radiology.* 2014;272(2):568-576.
24. Jamshidi N, Diehn M, Bredel M, Kuo MD. Illuminating radiogenomic characteristics of glioblastoma multiforme through integration of MR imaging, messenger RNA expression, and DNA copy number variation. *Radiology.* 2014;270(1):1-2.
25. Yamamoto S, Maki DD, Korn RL, Kuo MD. Radiogenomic analysis of breast cancer using MRI: a preliminary study to define the landscape. *AJR Am J Roentgenol.* 2012;199(3):654-663.
26. Langer DL, Kwast TH, Evans AJ, et al. Prostate tissue composition and MR measurements: investigating the relationships between ADC, T2, Ktrans, ve, and corresponding histologic features. *Radiology.* 2010;255(2):485-494.
27. Meyer F, Beucher S. *The Morphological Approach to Segmentation: The Watershed Transformation. Mathematical Morphology in Image Processing.* Boca Raton: CRC Press; 1993:49.
28. Tofts PS. Modeling tracer kinetics in dynamic Gd-DTPA MR imaging. *J Magn Reson Imaging.* 1997;7(1):91-101.
29. Signoretti S, Waltregny D, Dilks J, et al. p63 is a prostate basal cell marker and is required for prostate development. *Am J Pathol.* 2000;157(6):1769-1775.
30. Zhou M, Shah R, Shen R, Rubin MA. Basal cell cocktail (34betaE12 + p63) improves the detection of prostate basal cells. *Am J Surg Pathol.* 2003;27(3):365-371.
31. Xu J, Stolk JA, Zhang X, et al. Identification of differentially expressed genes in human prostate cancer using subtraction and microarray. *Cancer Res.* 2000;60(6):1677.
32. Welsh JB, Sapinoso LM, Su AI, et al. Analysis of gene expression identifies candidate markers and pharmacological targets in prostate cancer. *Cancer Res.* 2001;61(16):5974.
33. Rubin MA, Zhou M, Dhanasekaran SM, et al. alpha-methylacyl coenzyme A racemase as a tissue biomarker for prostate cancer. *JAMA.* 2002;287(13):1662-1670.
34. Padhani AR, Gapinski CJ, Macvicar DA, et al. Dynamic contrast enhanced MRI of prostate cancer: correlation with morphology and tumour stage, histological grade and PSA. *Clin Radiol.* 2000;55(2):99-109.
35. Rouvière O, Raudrant A, Ecochard R, et al. Characterization of time-enhancement curves of benign and malignant prostate tissue at dynamic MR imaging. *Eur Radiol.* 2003;13(5):931-942.
36. Xu J, Humphrey PA, Kibel AS, et al. Magnetic resonance diffusion characteristics of histologically defined prostate cancer in humans. *Magn Reson Med.* 2009;61(4):842-850.
37. Rosenkrantz AB, Sigmund EE, Johnson G, et al. Prostate cancer: feasibility and preliminary experience of a diffusional kurtosis model for detection and assessment of aggressiveness of peripheral zone cancer. *Radiology.* 2012;264(1):126-135.
38. Vos EK, Litjens GJS, Kobus T, et al. Assessment of prostate cancer aggressiveness using dynamic contrast-enhanced magnetic resonance imaging at 3 T. *Eur Urol.* 2013;64(3):448-455.
39. Rothke M, Blondin D, Schlemmer HP, Franiel T. [PI-RADS classification: structured reporting for MRI of the prostate]. *RoFo: Fortschritte auf dem Gebiete der Röntgenstrahlen und der Nuklearmedizin.* 2013;185(3):253-261.
40. Murray E, Cho JH, Goodwin D, et al. Simple, scalable proteomic imaging for high-dimensional profiling of intact systems. *Cell.* 2015;163(6):1500-1514.
41. Sylwestrak Emily L, Rajasethupathy P, Wright Matthew A, Jaffe A, Deisseroth K. Multiplexed intact-tissue transcriptional analysis at cellular resolution. *Cell.* 2016;164(4):792-804.
42. Gerlinger M, Rowan AJ, Horswell S, et al. Intratumor heterogeneity and branched evolution revealed by multiregion sequencing. *N Engl J Med.* 2012;366(10):883-892.
43. Gerlinger M, Swanton C. How Darwinian models inform therapeutic failure initiated by clonal heterogeneity in cancer medicine. *Br J Cancer.* 2010;103(8):1139-1143.
44. Navin N, Kendall J, Troge J, et al. Tumour evolution inferred by single-cell sequencing. *Nature.* 2011;472(7341):90-94.

## SUPPORTING INFORMATION

Additional Supporting Information may be found online in the supporting information tab for this article.

**How to cite this article:** Cipollari S, Jamshidi N, Du L, et al. Tissue clearing techniques for three-dimensional optical imaging of intact human prostate and correlations with multiparametric MRI. *The Prostate.* 2021;81:521-529. <https://doi.org/10.1002/pros.24129>